

This item is the archived peer-reviewed author-version of:

Real-time structured light-based otoscopy for quantitative measurement of eardrum deformation

Reference:

van der Jeught Sam, Dirckx Joris.- Real-time structured light-based otoscopy for quantitative measurement of eardrum deformation

Journal of biomedical optics / SPIE: International Society for Optical Engineering; International Biomedical Optics Society - ISSN 1083-3668 - 22:1(2017), p. 1-32

Full text (Publishers DOI): <http://dx.doi.org/doi:10.1117/1.JBO.22.1.016008>

To cite this reference: <http://hdl.handle.net/10067/1395360151162165141>

Real-time structured light-based otoscopy for quantitative measurement of eardrum deformation

Sam Van der Jeught^{a,*}, Joris JJ Dirckx^a

^aUniversity of Antwerp, Department of Physics, Laboratory of Biomedical Physics, Groenenborgerlaan 171, B-2020 Antwerp, Belgium

Abstract. A new otological profilometry device based on real-time structured light triangulation is presented. A clinical otoscope head is mounted onto a custom handheld unit containing both a small digital light projector and a high-speed digital camera. Digital fringe patterns are projected onto the eardrum surface and are recorded at a rate of 120 unique frames per second. The relative angle between projection and camera axes causes the projected patterns to appear deformed by the eardrum shape, allowing its full-field three-dimensional surface map to be reconstructed. By combining hardware triggering between projector and camera with a dedicated parallel processing pipeline, the proposed system is capable of acquiring a live stream of point clouds of over 300.000 data points per frame at a rate of 40 Hz. Real-time eardrum profilometry adds an additional dimension of depth to the standard 2D otoscopy image and provides a non-invasive tool to enhance the qualitative depth perception of the clinical operator with quantitative 3D data. Visualization of the eardrum from different perspectives can improve the diagnosis of existing and the detection of impending middle ear pathology. The capability of the device to detect small middle ear pressure changes by monitoring eardrum deformation in real-time is demonstrated.

Keywords: otoscopy; tympanic membrane; profilometry; real-time; graphics processing unit

*Sam Van der Jeught, E-mail: sam.vanderjeught@uantwerpen.be

1 Introduction

The tympanic membrane (TM) or eardrum is a thin membrane that separates the middle ear from the external ear. Besides conducting sound wave vibrations from air to the ossicles, the tympanic membrane protects the middle ear from external influences which may cause infections. The three-dimensional, conical shape of the TM plays a crucial role in this process and any structural change to its topography can be an indicator for existing or impending pathology. In the following, we will refer to the measurement of the tympanic membrane surface shape as *tympano-topography*.

35 Currently, primary clinical diagnosis of middle ear inflammation or otitis media is carried out
36 using a standard otoscope. In the otoscope head, a magnifying lens is placed directly behind a
37 disposable speculum, allowing for visual inspection of the ear canal and the external side of the
38 tympanic membrane. While this generally suffices for the detection of visually observable
39 defects such as tympanic membrane ruptures, retraction pockets or inflammation of the
40 cutaneous layer, otoscopic examination is limited to 2D visualization of the eardrum structure
41 only, and no information on structurally less discernible abnormalities can be generated. By
42 extending the two-dimensional qualitative view of the tympanic membrane with real-time 3D
43 surface shape information, a new dimension of quantitative data is made available to the
44 operator, which may support correct diagnosis of currently manifested pathology and open up a
45 new area of predictive otological diagnostics.

46 Due to the relatively small dimensions of the human tympanic membrane (8-10 mm diameter, 1-
47 2 mm apex height), measuring the dynamic deformation of its 3D surface shape in-vivo with
48 sufficiently high resolution is not a trivial task. Recent reports of optical coherence tomography
49 (OCT) systems have demonstrated the capability of the technique to measure human tympanic
50 membrane thickness in-vivo and in real-time by delivering and collecting the light through a
51 handheld probe^{1,2}. Although additional data on the internal structure of the membrane is
52 generated this way, extracting the 3D surface shape model from the axial depth scans requires
53 full-field segmentation which is typically done in post-processing. In addition, the required
54 broadband light source reduces portability of the otoscopic OCT system. Alternatively, digital
55 holography has been used to measure micro-deformations and 3D vibrational (sound-induced)
56 motion of tympanic membranes^{3,4} using double-exposure, multiple-wavelength techniques, but
57 sub-wavelength stability of the measurement sample is required between subsequent exposures.

58 Recently, we have developed a real-time microscopic profilometry system⁵ capable of acquiring
59 30 microscopic height maps per second with depth resolutions in the micrometer range by
60 projecting structured light patterns onto the object surface through one optical pathway of a
61 stereoscopic operation microscope and by recording the deformed patterns through the second
62 pathway. Although this resulted in high-quality 3D maps of the object surface with depth
63 resolution in the order of 10 micrometers, a rather large working distance of 200-415 mm from
64 object lens to target surface was required. Unfortunately, the human ear canal has a sigmoid
65 shape and straight optical passage to the tympanic membrane cannot always be guaranteed.
66 Similarly, a number of other medical procedures suffer to extract 3D information directly from
67 optically inaccessible human tissue due to anatomical limitations. These include the family of
68 minimally invasive laparoscopic surgery techniques employed during gallbladder removal⁶,
69 hernia repair⁷, removal of part of the colon or small intestine⁸, removal of the spleen⁹, removal of
70 the adrenal glands¹⁰ and removal of the kidneys¹¹. Although correct three-dimensional
71 orientation is critical in these procedures, the operator is typically provided only with a live feed
72 of 2D images. In order to provide the laparoscopic surgeon with better depth perception, marker-
73 less tracking systems have been designed to align the real-time video feed to preoperatively
74 recorded 3D-CT scans of the tissue surface as an overlaid augmented display¹². Depth accuracy
75 of these supplementing tracking systems is limited, since they rely on prerecorded measurements
76 and provide no direct, real-time feedback on the current topology of the observed tissue.
77 To this end, recent efforts have been made to integrate optical profilometry systems into
78 miniaturized 3D otoscopic and endoscopic devices. The first stereoscopic endoscopy systems
79 illuminated the object surface with uniform light and imaged the scene using a dual sensor setup.
80 This was achieved by employing either two imaging sensor chips with two distinct lenses¹³ or by

81 employing a single lens behind two pupil openings combined with a lenticular array and a single
82 imaging sensor^{14,15}. Either way, 3D data was extracted from the dual-viewpoint images by
83 solving the correspondence problem. The quality of this technique is known to depend heavily
84 on the optical structure of the imaged scene and suffers from featureless areas or shadow effects.
85 Alternatively, the correspondence problem can be solved by replacing one of the two imaging
86 sensors with a light source that projects predefined structured light patterns onto the scene. This
87 way, triangulation can be performed directly by virtually intersecting the projected and the
88 intercepted light rays using custom reconstruction algorithms.

89 In endoscopy, the narrow size of the sensor head and the small diameter of the attached flexible
90 shaft complicate the design of the device optics that are required for projection and recording of
91 the fringe patterns. As size constraints prohibit implementation of a digital light projector unit
92 into the sensor head itself, light is typically generated remotely outside of the endoscope and
93 supplied through glass fibers. In order to solve the correspondence problem, the projected light
94 must be provided with position-dependent and uniquely identifiable markers. One way to
95 landmark the object surface is to illuminate the scene with a grid of dots of multiple
96 wavelengths¹⁶. After identification of these dots in the camera image, the correspondence
97 problem can be solved and 3D reconstruction of the object surface can be performed. This
98 technique is highly sensitive to the dynamic range and color resolution of the employed CCD
99 chip and produces 3D point clouds of limited density. Another way to install codification into the
100 projected light beams is to pass the light through a ring-shaped slide placed in the sensor head,
101 generating colored cones around the central endoscope axis in a circular pattern¹⁷. While this
102 design is optimized for imaging of tubular cavities, no 3D information of the object scene in
103 front of the endoscope head is generated. Alternatively, dual-barrel systems with separate

104 endoscopes for illumination and observation have been proposed¹⁸, but these result in large and
105 impractical setups and are generally unsuited for common medical applications. A detailed
106 overview of 3D endoscopic systems can be found in^{19,20}.

107 In otoscopy, the limited penetration depth of the scanner head imposes fewer dimensional
108 restrictions onto the otoscopic device than is the case in standard endoscopy. As the human ear
109 canal has an average length of about 25 mm and a diameter of 7 mm, the eardrum can generally
110 be monitored in its entirety by inserting a funnel-shaped speculum into the canal. Recently, a
111 light field otoscope has been reported that uses a microlens array in combination with a main
112 imaging lens placed directly behind the speculum to capture both the intensity and angular
113 distribution of light rays coming from the eardrum surface²¹. The plenoptic camera-based setup
114 allows submillimeter resolution height maps of the tympanic membrane to be constructed.
115 Although this technique does provide the operator with shape estimation of the eardrum under
116 static conditions, the depth precision is insufficient to quantify local deformations of the
117 membrane or to measure dynamic effects. More recently, Das et al.²² proposed a structured light-
118 based otoscopic device capable of achieving depth resolutions in the order of 20-30 μm . Their
119 prototype contains a portable LED projector for the projection of structured light patterns onto
120 the eardrum and a telephoto lens arrangement whose output is coupled to a webcam sensor. The
121 conical shape of the speculum enables a small angle between projection and recording axis to be
122 made and the 3D otoscopic device optics to be redesigned into a new, compact device. Since Das
123 et al. employed multi-phase structured light profilometry in combination with a low-end
124 projector-camera system, recording and visualization of height maps required 1.5 seconds per
125 measurement. This relatively long acquisition time not only reduces the height measurement

126 precision due to patient or operator movement, it also inhibits monitoring of dynamic eardrum
127 deformation.

128 Both the detection of weak spots on the eardrum and the evaluation of Eustachian tube
129 functioning require 3D shape data of the TM to be gathered when varying pressures are applied
130 over the membrane. As pressure stabilization is a dynamic process²³, multiple intermediate
131 measurements are required and real-time feedback of the TM surface shape change is needed. In
132 the following, we present a new 3D otoscopic handheld device containing a real-time structured
133 light triangulation engine with custom triggering between projection and camera hardware and a
134 dedicated digital signal processing pipeline based on graphics processor unit programming. By
135 using a digital light projector (DLP) with configurable digital micromirror displays (DMD's),
136 any single-or multi-shot structured light profilometry technique can be employed. This way, the
137 pixel period of projected fringes or the number of total phase-shifted frames per 3D measurement
138 can easily be modified, depending on the reflectivity profile of the object surface, the required
139 depth resolution and the minimum 3D frame rate. The 3D otoscope generates a live stream of 40
140 full-field surface maps per second, each containing a point cloud of 300.000 data points per
141 frame. For a comprehensive overview of current state-of-the-art real-time structured light
142 profilometry techniques, we direct the reader to Zhang²⁴ and Van der Jeught²⁵.

143 The paper is organized as follows: the next section presents the experimental setup and outlines
144 the technical aspects of the device. A brief overview of the parallel digital signal processing
145 pipeline and the employed structured light profilometry technique is given. Section 3
146 demonstrates the experimental results of the 3D otoscopic device, including measurements of
147 calibration samples with known topographies and an ex-vivo tympanic membrane. Section 4

148 discusses important aspects of the hardware setup and the employed algorithms and explores the
149 transition of the device into the clinical setup. Finally, section 5 concludes the paper.

150 **2 Methods**

151 *2.1 Experimental setup*

152 A standard clinical otoscope was used as the base optical setup for our real-time 3D scanning
153 device. In its standard configuration, the otoscope consists of a handle and a head with at its
154 distal end an attachment for disposable plastic specula. Uniform white light is generated in an
155 LED module located inside the otoscope handle and is injected into the ear canal via a plastic
156 mirror. The light which is reflected from the tympanic membrane is focused onto the observer
157 eye by a 3× magnifying lens placed at the rear of the head.

158 In order to provide the otoscopic device with digital fringe projection and 3D data extraction
159 capabilities, several modifications to its optical configuration were implemented. First, the LED
160 module and the entire otoscope handle were removed from the otoscope head. The plastic mirror
161 was replaced by a semi-transparent mirror which was installed inside the otoscope head at a 40°-
162 45° angle between central speculum axis and former handle shaft. Next, a custom handheld
163 aluminum frame was designed to align a high-speed CCD sensor (Imperx IGV-B0620M, 210
164 frames per second, 640 × 480 pixels, 12-bit grayscale images) perpendicularly to the prior
165 otoscope handle axis. Finally, the magnifying lens was removed and a Texas Instruments
166 Lightcrafter pico-projector evaluation module was installed at the rear of the otoscope head. The
167 modified otoscopic unit and a schematic overview of its optical layout are shown in Fig. 1. In its
168 entirety, the prototype weighs around 800 grams and can easily be held in one hand. The device
169 is powered and connected to the PC only through flexible cables and can easily be maneuvered

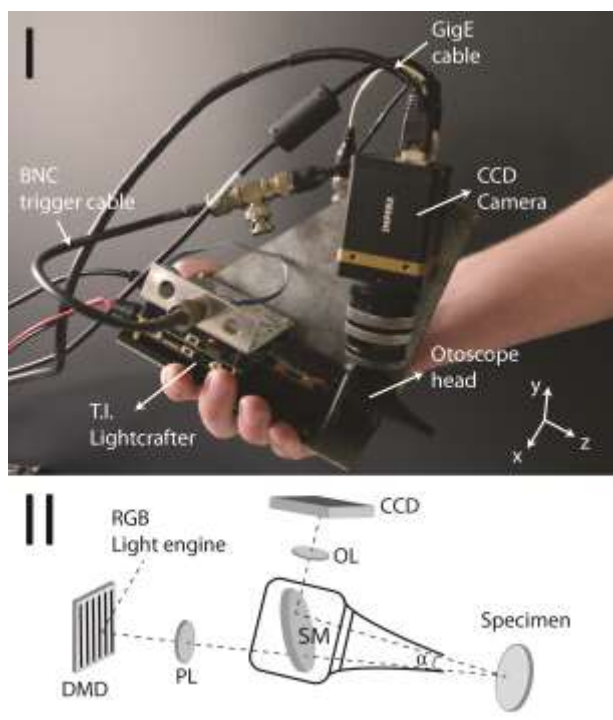
170 under any angle. Nevertheless, future iterations of the hardware design will include more detail
171 to ergonomics and form factor.

172 Uniform red, green or blue light is generated by the RGB-LED light engine inside the Texas
173 Instruments (T.I.) Lightcrafter module and reaches the digital micromirror device (DMD) under
174 a fixed angle. The light is reflected by the individually rotating micromirrors into a pixelated
175 (608×684 -pixel) grayscale fringe pattern that is projected onto the object surface after passing
176 the projector lens (PL) and the semi-transparent mirror (SM). The deformed fringe pattern is
177 observed by the CCD sensor after being reflected on the SM and after passing the observation
178 lens (OL). The BNC cable enables triggering between CCD and DMD and the recorded fringe
179 patterns are transferred from CCD memory to RAM memory using the Gigabit Ethernet (GigE)
180 interface.

181 The T.I. Lightcrafter module is a compact (116 mm x 65 mm) DLP-based light projection system
182 containing flash memory for on-board pattern and sequence storage. It generates 8-bit grayscale
183 patterns at a rate of 120Hz and binary patterns at a rate of 4kHz. The pico-projector and its
184 focusing lens system was oriented so that the central projection axis of the projected images
185 enter the head under an angle of $\alpha = 20^\circ$ relative to the observation axis. This angle between
186 projection and observation axes causes the projected fringe patterns to appear deformed by the
187 object shape and allows the 3D object surface data to be extracted.

188 The duty cycle of the rapidly rotating micromirrors determines the amount of light that is
189 reflected towards the output and therefore sets the grayscale intensity per pixel. In contrast to
190 commercial video projectors, which adopt nonlinear duty cycles for better subjective visual
191 effect, the Lightcrafter module is designed to maintain a linear relation between input and output
192 grayscale intensity or ‘gamma-curve’. The micromirror duty cycle is divided discretely into eight

193 bit-planes, each representing a fraction between one half and 1/256th of the total illumination
 194 time. Therefore, to avoid visual artifacts, it is important that the projector-camera system is
 195 synchronized to record integer multiples of the total illumination time only. To ensure proper
 196 triggering, custom-made electronics were built to connect the trigger output of the Lightcrafter
 197 logic board to the high-speed camera, and the camera exposure time was set to the interval
 198 between successive trigger pulses, corresponding to 1/120th of a second or 8.33 ms per image
 199 capture.



200
 201 **Fig. 1** Modified otoscopic unit (I) and schematic overview of its optical layout with enlarged
 202 detail of otoscope head (II).
 203

204 *2.2 Real-time digital signal processing pipeline*

205 The digital nature of the DLP unit allows us to implement any structured light projection
 206 technique in the otoscopic profilometer. Without loss of generality, in the following we describe

207 the implementation of the standard three-phase 2+1 technique²⁶. This technique requires only
 208 three unique intensity images per 3D measurement and therefore allows a high 3D frame rate to
 209 be obtained. For a similar description of four-phase fringe pattern pipelines, we direct the reader
 210 to Van der Jeught et al⁵.

211 Before acquisition, three preconstructed 8-bit digital patterns are uploaded to the on-board flash
 212 memory of the Lightcrafter module and are displayed in a loop: two line patterns with
 213 sinusoidally varying intensity distribution and a relative phase shift of $\pi/2$, and a single uniform
 214 white image. When observed by the camera under a relative angle with the projection axis, these
 215 line patterns appear deformed by the object shape and can be described as

$$216 \quad I_1(i, j) = I'(i, j) + I''(i, j) \sin\{\varphi(i, j)\} \quad (1)$$

$$217 \quad I_2(i, j) = I'(i, j) + I''(i, j) \cos\{\varphi(i, j)\} \quad (2)$$

$$218 \quad I_3(i, j) = I'(i, j) \quad (3)$$

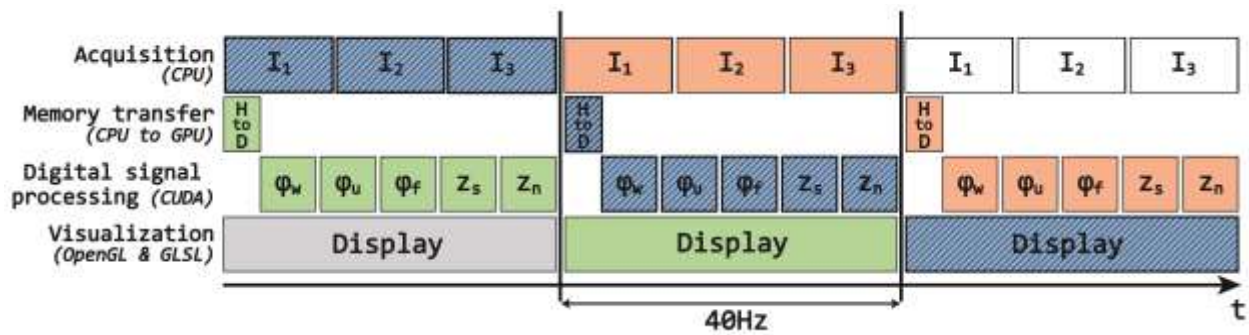
219 with $I_{1-3}(i, j)$ the three deformed intensity patterns at pixel indices i and j , I' the average or
 220 background intensity, I'' the intensity profile modulation or fringe pattern amplitude, and $\varphi(i, j)$
 221 the phase map of the deformed fringe pattern sequence. The phase map can be obtained by
 222 solving Eqs. (1-3):

$$223 \quad \varphi(i, j) = \tan^{-1} \left(\frac{I_1 - I_3}{I_2 - I_3} \right) \quad (4)$$

224 The phase φ is now extracted from the three input intensity images and can be linked directly to
 225 the local object height z through proper calibration and scaling and by removing the artificial 2π
 226 discontinuity jumps that originate from the limited principle value domain $]-\pi, \pi]$ of the
 227 arctangent function.

228 In order to achieve real-time display of 3D height maps, several optimization techniques were
 229 employed in the proposed setup. First, acquisition, digital signal processing and visualization of

230 height maps are executed simultaneously in an asynchronous workload organization. Second, all
 231 digital signal processing components themselves are designed to operate in parallel on the
 232 graphics processing unit (GPU) of a standard graphics card. Third, GPU interoperability between
 233 parallel data processing interface CUDA (Compute Unified Device Architecture) and
 234 visualization interfaces OpenGL and GLSL was established to minimize data transfers across the
 235 PCI bus and to relieve the CPU from most computationally intensive tasks. The entire software
 236 library, from data acquisition to onscreen rendering of 3D measurement results, was written in
 237 custom C++-based code to ensure optimal data flow control and memory management. The
 238 digital signal processing pipeline was executed on a commercial GTX980 graphics card with
 239 3072 CUDA cores and 4096MB of on-board GDDR5 RAM memory.



240
 241 **Fig. 2** (color online) Real-time three-step 2+1-phase shifting profilometry timeline. Horizontally
 242 aligned blocks occur sequentially; vertically aligned blocks occur simultaneously. At all times,
 243 fringe pattern acquisition, digital signal processing and on-screen rendering of successive
 244 measurements are executed asynchronously. Following the data processing cycle of one 3D-
 245 measurement (blue, diagonally hatched), three input fringe patterns are first captured by the
 246 high-speed camera and transferred from CPU to GPU memory. Next, the digital signal
 247 processing pipeline performs successive wrapped phase extraction (ϕ_w), phase unwrapping

248 (φ_U) , Gaussian filtering (φ_f), phase-to-height conversion and scaling (z_S) and normal
249 calculation (z_N). Finally, the 3D height map is rendered and displayed.

250

251 A more detailed schematic overview of the real-time 2+1-phase profilometry pipeline is
252 presented in Fig. 2. Input fringe patterns I_{1-3} are acquired continuously and are downloaded
253 from the camera data buffer in blocks of three. This process is supported by hardware triggering
254 and controlled by the CPU. Simultaneously, the previous block of fringe patterns is transferred
255 from host (CPU) to device (GPU) memory where the 12-bit grayscale input images are stored as
256 2-byte unsigned integer texture arrays. Next, control over the data processing pipeline is passed
257 over to the GPU and the CPU returns to data acquisition control. The first step in the digital
258 signal processing pipeline is the extraction of the wrapped phase φ_W from the three input fringe
259 patterns using Equation (4). As the phase of neighboring pixels can be calculated independently,
260 this process is highly suited for parallel implementation. Next, the original, continuous phase
261 signal φ_U is recovered by adding an integer multiple of 2π to every phase value of the wrapped
262 phase grid φ_W in a process commonly referred to as two-dimensional phase unwrapping²⁷. A
263 3×3 Gaussian filter kernel is applied to the unwrapped phase array to reduce spikes caused by
264 motion or system noise and the filtered phase values φ_f are converted to actual 3D Euclidian
265 coordinates by applying the reference-plane-based calibration approach²⁸. After recording the
266 phase grid of a reference plane φ_R where the base-plane depth is set to $z = 0$, the difference
267 between φ_R and subsequent phase measurements is proportional to the object depth z by some
268 constant scaling value. This scaling value z_S can then easily be obtained from calibration
269 measurements on an object of known dimensions. Finally, point normals to the vertex geometry
270 z_N are calculated by taking the cross products of neighboring phase value gradients so that Phong

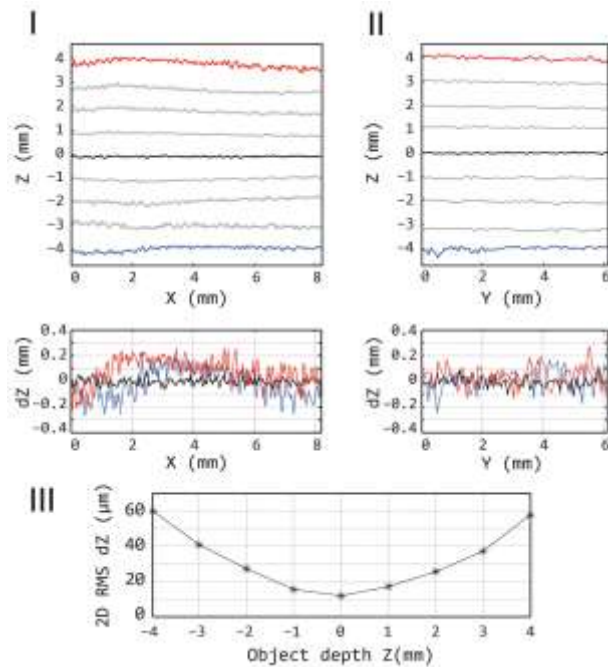
271 lighting²⁹ may be applied in 3D visualization mode. Note that the digital signal processing blocks
272 as illustrated in Fig. 2 are not scaled to represent the respective time they take, but are in fact
273 expanded to fill the maximum time slot they could take up without obstructing the real-time
274 pipeline. In reality, the entire digital signal processing of the three images, including memory
275 transfer from host to device, takes up only 11.2 ms in total.

276 The GPU-calculated height measurements are visualized from GPU memory and no additional
277 device-to-host memory transfers are needed. For final rendering of the result, two graphics
278 application programming interfaces (API's) are employed: OpenGL and GLSL. In order to allow
279 off-screen rendering, i.e. the drawing of scenes into buffers other than the frame or screen buffer,
280 a standard double buffering technique is employed. To this end, an additional OpenGL frame
281 buffer object (FBO) is created as backbuffer and its output is bound to GPU texture memory.
282 Only when the backbuffer is fully rendered, it is swapped with the screen-or frontbuffer,
283 effectively hiding the rendering process from the user whilst minimizing latency. For final
284 display, three small shader programs are written in the OpenGL shading language GLSL. The
285 first one incorporates the previously calculated point normals in a 3D Phong light reflection
286 model, computing the virtual illumination brightness and color of the object surface pixel per
287 pixel, depending on user-defined variables such as object surface reflectance and 3D position of
288 light source and observer. The second one converts the height values to a pixel color using a
289 predefined color map, generating a 2D color-coded height map which is projected onto the object
290 surface for quick assessment of object topography. The third one projects the uniform bright
291 image that was gathered in the acquisition step of the 2+1-phase technique onto the object
292 surface. This shader program enhances operator orientation as object texture features which
293 cannot be resolved as height differences are incorporated into the final 3D result, also.

294 **3 Results**

295 *3.1 Measurement precision*

296 To determine the depth resolution of the proposed otoscopic profilometry setup, the surface
297 profile of a flat glass plate was measured at various discrete distance intervals around the central
298 focal plane. Pregenerated structured light patterns with a sinusoidal intensity profile of 24 pixels
299 per fringe period were projected onto the glass plate surface. The glass plate itself was mounted
300 onto a translation stage which allowed displacement along the projection (or Z-) axis. The
301 projected fringe patterns spanned a field of view of 8.15 x 6.11 mm across the glass plate
302 surface, which was coated with magnesium oxide to ensure good diffuse reflectivity. Cross-
303 sections of these measurements along the central pixel lines in both X-and Y-dimensions are
304 shown in the top row of Fig. 3. The numerical difference between these cross-sections at depths
305 of $Z = +4$ mm (red), $Z = 0$ mm (black) and $Z = -4$ mm (blue) around the central focal plane
306 are included in the second row. No Gaussian smoothing was applied to the 3D data.



307

308 **Fig. 3** The surface profile of a flat glass plate was measured at discrete intervals around the
309 central focal plane $Z = 0$ to determine the measurement precision of the proposed otoscopic
310 system. Cross-sections of these depth measurements along the X -axis (I) and the Y -axis (II) are
311 included in the first row, and the corresponding depth measurement errors (dZ) at object depths
312 of $Z = +4$ mm (red), $Z = 0$ mm (black) and $Z = -4$ mm (blue) are included in the second row.
313 Part III plots the two-dimensional root-mean-square values of the difference between the full flat
314 glass plate measurements and their respective best planar fits in function of object depth.

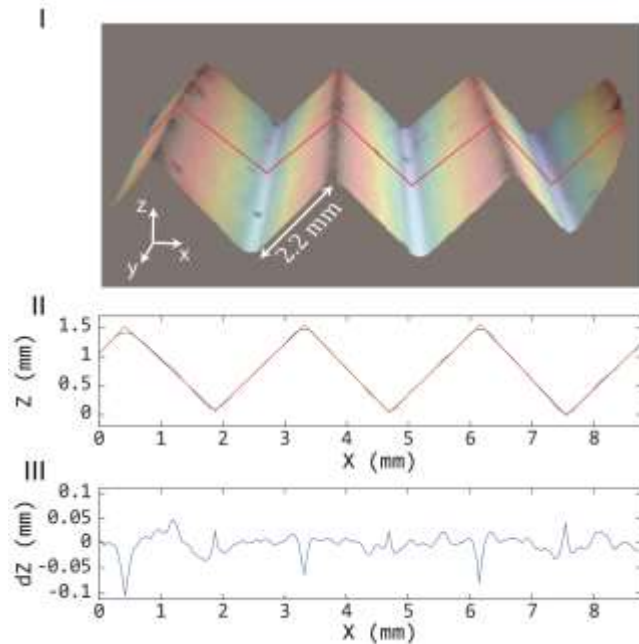
315
316 It can be seen that measurement precision decreases with increasing distance of the object to the
317 focal plane. This effect is standard for structured light projection techniques is due to the fact that
318 the contrast of the projected fringe patterns deteriorates away from the focal plane due to
319 defocusing effects. With decreasing fringe pattern contrast, the intensity values $I_{1-3}(i, j)$ in Eq.
320 (4) converge towards each other. This reduces the numerical digital range of the intensity ratio
321 formula used to calculate the phase $\varphi(i, j)$ and limits the measurement resolution of the
322 technique. Furthermore, it should be noted that the projection optics of the T.I. Lightcrafter
323 module are designed for asymmetric upwards projection. When the projected fringe patterns
324 reach the object surface outside of the focal plane, they contain a certain amount of geometric
325 distortion relative to the angle between the normal of the object surface and the central projection
326 axis. The accumulated measurement errors due to fringe pattern defocus and geometric distortion
327 artifacts largely remain within a region of $dZ = \pm 200 \mu\text{m}$.

328 In order to quantize the system's mean measurement error as a function of object depth, the full-
329 field two-dimensional root-mean-square (2D-RMS) values of the differences between the flat
330 plate measurements at each depth interval and their respective best 2D plane fits are plotted in

331 part III of Fig. 3. From this plot, axial resolution of 3D measurements can be determined, given
332 the total object depth span and assuming that the object is placed centrally around the focal
333 plane. The measurement error in depth (dZ) increases with distance away from the central focal
334 plane, though remains below an RMS of $60\ \mu\text{m}$ within a region of $\pm 4\ \text{mm}$ around $Z = 0$.

335 *3.2 Calibration standard and live visualization software*

336 To demonstrate the real-time digital signal processing and visualization engine of the proposed
337 otoscopic profilometry setup, a calibration standard with right-angled triangular ridges of $2.2\ \text{mm}$
338 deep was measured. Again, the object was coated with magnesium oxide to ensure maximum
339 diffuse reflection and its height profile was distributed symmetrically around the focal plane. A
340 still frame from the live recorded measurement video (Vid. 1) is shown in part I of Fig. 4. The
341 central pixel line of the resulting 3D measurement is highlighted in red. The cross-section of the
342 height measurement along this central pixel line is illustrated in blue in part II with its segmented
343 linear fit overlaid in red. The numerical difference between height measurement and linear fit is
344 included in part III.



345

346 **Fig. 4, Vid. 1** Still frame from live measurement video demonstrating the real-time otoscopic
 347 profilometry technique (I), including a cross-section of the object's height profile Z along the
 348 central pixel line (II) and its measurement error dZ (III).

349

350 As can be seen in the measurement video, the software allows the user to rotate the object in 3D
 351 perspective view and to control visualization effects such as colormap range, position of virtual
 352 light source relative to the observer and quality threshold of rendered height map data. The video
 353 stream was recorded directly from the computer screen using frame grabber software and was
 354 resampled from 40 fps to 29.97 fps in accordance with standard H.264 codec protocol. During
 355 live measurement, the user is able to switch between custom shader programs designed to
 356 emphasize either the height profile or the texture of the object surface. For fast assessment of the
 357 object's height profile, the object vertices are each assigned a color ranging from blue (low Z -
 358 value) to red (high Z -value). Alternatively, the shader can superimpose the uniformly lit input
 359 intensity image onto the object surface to incorporate texture features in the 3D model. Finally, a

360 blend or combination of these two shader programs can be selected, which is shown in the first
361 part of Vid. 1 and in part I of Fig. 4.

362 In order to reduce high-frequency phase noise during live measurements, a 3×3 Gaussian filter
363 is applied to the unwrapped 3D data. As a result, the 3D geometry is smoothed out and sharp
364 corners become rounded. This effect can be seen clearly in part II and III of Fig. 4 when
365 measuring the right-angled indentations of the calibration standard. The measurement noise stays
366 well within $dZ = \pm 50 \mu\text{m}$, except at the borders between successive segmented lines where the
367 height measurements deviate up to $dZ = \pm 100 \mu\text{m}$ from the linear fit. Since the otoscopic
368 profilometer was designed mainly to measure the surface profile of human tympanic membranes
369 which typically possess a smooth 3D tent-like shape and generally do not contain features with
370 edged transitions, rounding artefacts of sharp angles do not impede the intended 3D TM shape
371 measurements. Nevertheless, the Gaussian filter is optional and can easily be omitted from the
372 digital signal processing pipeline by the user during live measurement.

373 *3.3 Dynamic pressurization of tympanic membrane ex-vivo*

374 As a first step towards implementation of real-time tympano-topography in the clinical ENT
375 office, the otoscopic profilometer was used to measure the 3D shape distortion of an ex-vivo
376 tympanic membrane caused by dynamic pressurization. A fresh (frozen) temporal bone was
377 obtained from the Life Legacy Foundation and the tympanic membrane remained in-situ during
378 the measurements. To mimic an in-vivo measurement setup, the ear canal was left intact and the
379 tympanic membrane was optically accessible only by inserting a plastic speculum into the ear
380 canal. A small drop of water base cosmetic dye was used to coat the tympanic membrane with a
381 diffusely reflecting white layer. The middle ear cavity was (de-)pressurized by inserting a small
382 tube through one of the mastoid cells and by sealing the remainder of the mastoid cells airtight

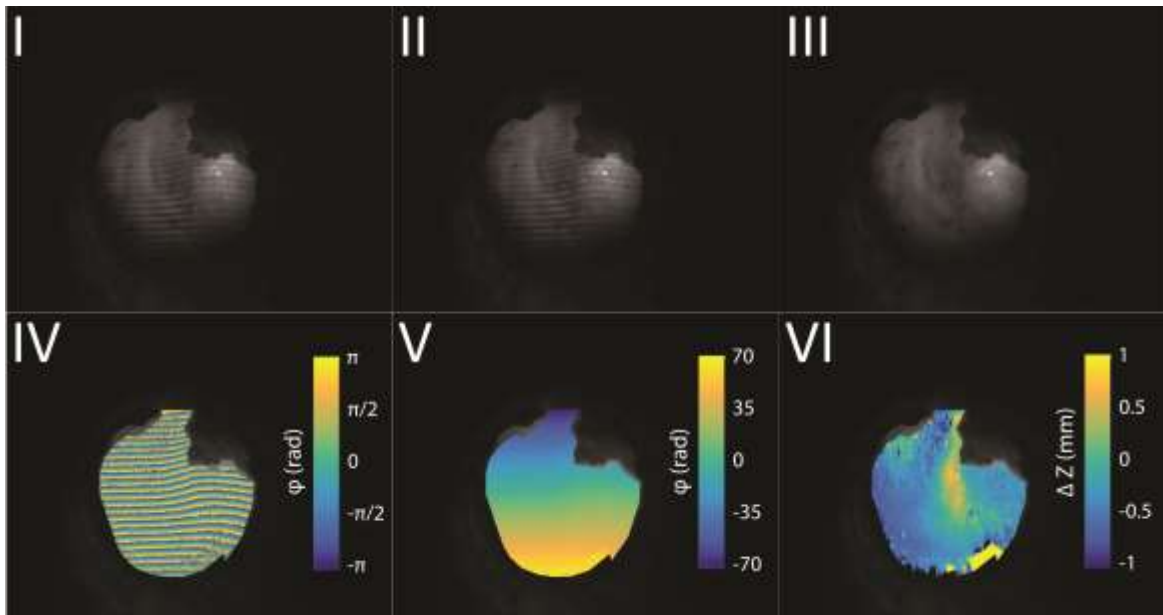
383 using two-component silicon paste. The air tube was connected to a pressure generator which
384 was controlled manually. The measurement setup is shown in Fig. 5.



385
386 **Fig. 5** Dynamic tympano-topography measurement setup. The otoscopic profilometer head
387 contains a disposable speculum, which is inserted into the ear canal of an airtight sealed temporal
388 bone. The middle ear cavity is pressurized by connecting a small tube through one of the mastoid
389 cells to a pressure generator (not shown here).

390
391 Dynamic pressurization of the tympanic membrane was established by alternating the middle
392 ear cavity pressure between -0.4 kPa and +0.4 kPa several times over the course of a 7.1-second
393 measurement period. The 2 + 1 phase shifting profilometry technique was used to monitor the
394 3D deformation of the tympanic membrane shape in real-time and the measurement results were
395 downloaded to CPU RAM memory buffers and stored in computer memory for post-processing
396 and analysis purposes. Fig. 6 illustrates the various steps in the reconstruction process as it is
397 applied to one of the 284 sets of 3 input intensity images (Parts I-III). Two of these images
398 contain sinusoidally varying intensity profiles with a relative phase shift of $\pi/2$ and the third one
399 has a uniform intensity profile. Together, they can be combined to form a phase map of the

400 object (Part IV) from which the height profile is constructed after removal of the 2π -
 401 discontinuities (Part V). Next, the phase values are converted to absolute height values, Gaussian
 402 filtering is applied to the 3D geometry, and a reference map is deducted from the resulting height
 403 map. As we are interested in monitoring the 3D shape deformation of the membrane when
 404 pressure is applied over it, we have chosen to assign the first unwrapped phase map of the
 405 measurement stream (at pressure 0 kPa) as the default reference geometry to be subtracted from
 406 the subsequent phase maps. The resulting height deformation maps (Part VI) are therefore to be
 407 interpreted relative to zero-pressurization.



409 **Fig. 6** Various steps of the 2+1 phase shifting profilometry pipeline during measurement of
 410 tympanic membrane (left ear, medial view) shape deformation. Parts I-III: input intensity
 411 images; Part IV: wrapped phase map; Part V: unwrapped phase map; Part VI: height deformation
 412 map.

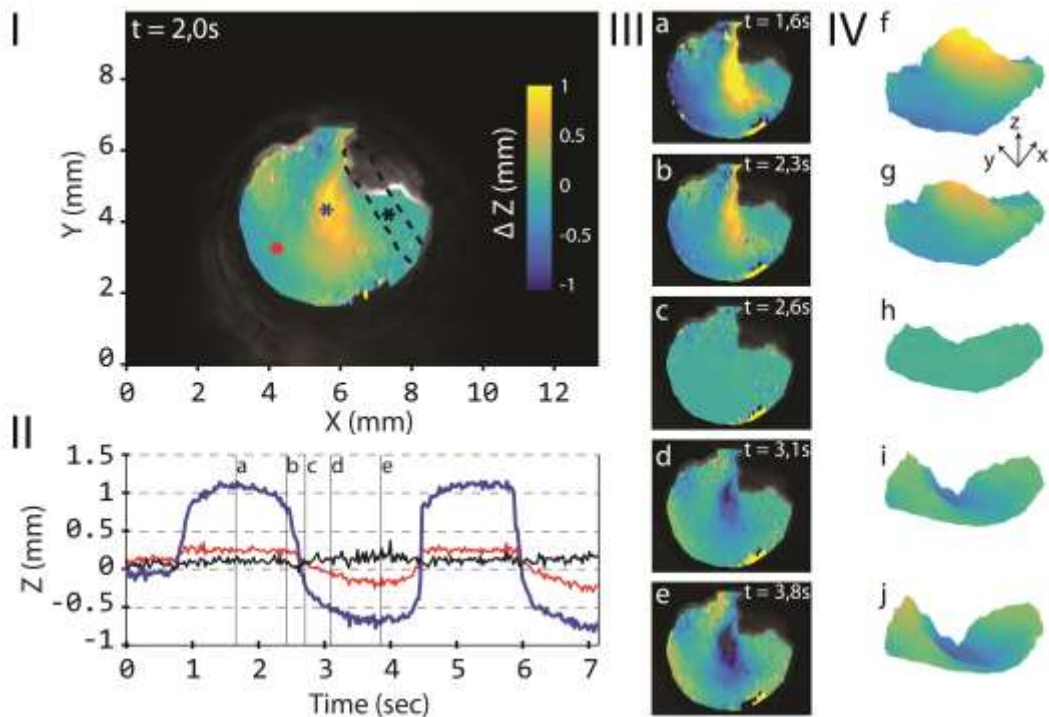
413
 414 It should be noted that a quality map is constructed in real-time for every trio of input
 415 intensity patterns by calculating the intensity modulation (the I'' -term in Eqs. 1 and 2) pixel-per-

416 pixel and by performing binary thresholding accordingly. This way, parts of the image that are
417 out of focus, contain shadows, are under-or over-exposed can be excluded from the phase map
418 and don't affect the resulting 3D measurement. However, the user is able to set outer limits to the
419 region of interest by marking the region with an interactive polygon, should manual intervention
420 be required. The quality map threshold value and the boundaries of the binary mask can be
421 modified in real-time during acquisition. Incorporation of the dynamic quality map in the
422 measurement pipeline increases the robustness of the technique during live measurement when
423 local structural irregularities (for example, the tissue of the ear canal partially blocking the view
424 of the tympanic membrane in the upper right side of the measurement sequence in Fig. 6) might
425 otherwise induce measurement artifacts in the reconstruction of the 3D phase map.

426 As illustrated in Fig. 7, the pressure change in the middle ear cavity results in height deformation
427 of the tympanic membrane. Part I shows the height deformation map of the TM when the applied
428 pressure was near maximum at +0.4 kPa over-pressure in the middle ear cavity. The manubrium
429 border of the malleus is marked by a dashed black line and three distinct locations on the
430 membrane surface along the manubrium (black), near the center of the posterior part of the pars
431 tensa (blue) and near the side of the pars tensa towards the annulus (red) are indicated by
432 asterisks. The corresponding height deformation profiles of the membrane at these locations are
433 plotted in function of time in Part II and reflect the pressure change cycles clearly. It can be seen
434 that the TM surface along the manubrium (black line) hardly moves during pressurization and
435 that maximum membrane deformation occurs towards the center of the pars tensa (blue line) and
436 to a lesser degree near the edge of the pars tensa (red line). This observation is confirmed by the
437 2D (Part III, a-e) and 3D (Part IV, f-j) visualizations of the full-field membrane height
438 deformation maps, plotted here at discrete intervals (*a-e*) during a pressurization cycle. A full

439 video of the eardrum deformation response is included in Vid. 2. The (semi-transparent) colored
 440 height deformation map is plotted on top of the input intensity image to illustrate the deformation
 441 of the projected line patterns on the moving object surface.

442 Since full-field phase maps are recorded, the user is able to monitor membrane deformation at
 443 any desired point on the observable TM surface. This way, the sensitivity of the technique to
 444 detect middle ear pressure variation can be maximized by monitoring the response curves of
 445 local areas on the TM that deform more than others. As the tympanic membrane expands up to 1
 446 millimeter when realistic pressure variations of 0.4 kPa are applied to over it, the system's
 447 measurement precision is more than sufficiently high to resolve the resulting deformation. Note
 448 the asymmetric response curve of the tympanic membrane topography as a function of induced
 449 pressure. The TM displacement induced by middle ear over-pressure is larger than for the
 450 corresponding under-pressure by a factor of almost 2. This effect was previously described by
 451 Dirckx et al.³⁰ and can be attributed to the conical shape of the membrane.



452

453 **Fig. 7** Tympanic membrane height deformation response to dynamic middle ear pressure
454 variation. Height deformation profiles and full-field 2D and 3D deformation maps are included
455 in Parts II, III and IV, respectively. The positive z-axis is defined towards the observer and the
456 colorbar legend defined in Part I applies to Parts III and IV, also.

457 **4 Discussion**

458 The *ex-vivo* TM measurements demonstrate the ability of the 3D otoscope to detect pressure
459 variations in the middle ear cavity by monitoring the 3D shape variation of the eardrum in real-
460 time. By asking patients to perform middle ear cavity (de)pressurization maneuvers such as the
461 Valsalva maneuver (forceful exhalation whilst closing one's mouth and nose), tympanic
462 membrane displacement can be measured and eardrum mobility can be quantified. Therefore, the
463 technique may have applications in the diagnosis of different pathologies encountered in the
464 ENT office.

465 For example, impeded mobility at the level of the eardrum may be used to detect certain
466 cases of otosclerosis or otospongiosis where fixation of the incudo-malleal or incudo-stapedial
467 joint reduces the mobility of the eardrum³¹.

468 Another application could be the detection of local elasticity variations in the tympanic
469 membrane. As aberrant local deformations or weak spots due to loss of stiffness of the TM could
470 indicate structural damage and be an important precursor for cholesteatoma formation³², a need
471 for quantitative evaluation of the full-field TM shape *in-vivo* has been expressed.

472 To link the pathophysiological mechanisms of chronic middle ear disease such as otitis
473 media with effusion (OME) to loss of TM stiffness, Dirckx et al. and von Unge et al. have
474 conducted a series of *ex-vivo* tympano-topography experiments on gerbil ears^{33,34}. By measuring
475 the 3D pressure-induced shape deformations of TMs with varying degrees of otitis media when

476 increasing levels of pressure were applied, a correlation between TM volume displacement and
477 stage of OME could be made. Therefore, as it has been shown that eardrum topography is a
478 valuable technique to quantify the stage of the disease, a real-time hand held device to measure
479 eardrum deformation may also find application in this field.

480 In addition to the detection of pathologies which result directly in aberrant eardrum mobility,
481 tympano-topography could also be employed as a non-invasive indicator for deficient Eustachian
482 tube (ET) functioning. Patients who suffer from obstructive ET-dysfunction lack a mechanism to
483 automatically equalize the air pressure in their middle ear cavity to the outside atmospheric
484 pressure. This leads to inadequate aeration of the middle ear and causes the eardrum to retract
485 inwards with possible destruction of the ossicular chain. Recently, a novel surgical technique to
486 treat obstructive ET dysfunction using a balloon catheter to stretch the ET was proposed³⁵.
487 Promising short-and intermediate-term results were confirmed by a study of Van Rompaey et
488 al.³⁶, indicating no complications within the first year after 41 catheter insertions in 26 patients.
489 Again, however, the authors stated that the first priority is to have an objective evidence-based
490 measurement technique to validate the long-term success of the proposed surgical procedure. To
491 this end, dynamic tympano-topography may provide a solution for early and quantitative
492 detection. By measuring the surface shape variation of the TM while patients are asked to
493 perform the Valsalva maneuver, pressure stabilization of the middle ear cavity and therefore
494 functioning of the ET can be evaluated objectively and quantitatively by monitoring the resulting
495 changes in TM surface volume.

496 Due to the digital nature of the projector-camera system, any structured light-based
497 profilometry technique can be implemented in the otoscopic profilometer. In this paper, we have
498 selected the 2 + 1 phase shifting technique for two main reasons. First, it requires only three

499 distinct input intensity images. This limits the acquisition time of a single 3D image to 25 ms for
500 our system, sufficiently brief to minimize motion artifacts due to patient or operator movement.
501 Second, the uniformly lit intensity image can be used in real-time during live measurements to
502 aid operator orientation when selecting the desired field-of-view on the TM surface.

503 Although the presented results provide a successful proof-of-principle of tympano-
504 topography as a non-invasive tool to monitor middle ear pressure change, several optimizations
505 to the otoscopic profilometry prototype system may be necessary before validation in the clinical
506 ENT office is in order. Currently, measurement resolution is limited by the 12-bit grayscale
507 range of the CCD-camera. Due to the semi-transparent nature of the TM structure, only a
508 fraction of the light projected onto the TM surface is reflected back. In order to improve the
509 measurement sensitivity, the CCD range needs to be divided into as many discrete grayscale bins
510 as possible. This can be achieved by either employing a camera sensor with a higher bit-range, or
511 by coating the TM surface with a diffusely reflecting dye, or both.

512 Finally, it is worth mentioning that since the object-to-lens distance in our system is much
513 larger than the observed depth variations themselves, the resulting geometric distortion artifacts
514 between object points closer to and further away from the otoscope head are very small when
515 compared to systems that employ wide-angle lenses close to the object surface (e.g. dual-barrel
516 endoscopic setups).

517 **5 Conclusion**

518 A novel otoscopic profilometry system based on structured light projection was developed and
519 experimentally tested. The handheld system is able to detect and quantify 3D eardrum
520 deformation caused by small middle ear pressure changes in real-time. Full-field height maps of
521 3D objects can be recorded at 40 frames per second with a measurement precision varying

522 between 10 and 100 μm , depending on local surface reflection parameters and total object depth
523 span. The device has a form factor similar to existing otoscopes, is easy to use and provides a
524 first step towards implementation of quantitative tympano-topography in the clinical ENT office.

525 **Acknowledgment**

526 The authors thank the Research Foundation - Flanders (FWO) for their financial support. The
527 authors have no relevant financial interests in the manuscript and no other potential conflicts of
528 interest to disclose.

529

530 **References**

- 531 1. R. L. Shelton et al., “Optical coherence tomography for advanced screening in the primary
532 care office,” *J. Biophotonics* **7**(7), 525–533 (2014) [doi:10.1002/jbio.201200243].
- 533 2. Z. Hubler et al., “Real-time automated thickness measurement of the in vivo human
534 tympanic membrane using optical coherence tomography,” *Quant. Imaging Med. Surg.*
535 **5**(1), 69–77 (2015) [doi:10.3978/j.issn.2223-4292.2014.11.32].
- 536 3. S. M. Solís, F. M. Santoyo, and M. D. S. Hernández-Montes, “3D displacement
537 measurements of the tympanic membrane with digital holographic interferometry,” *Opt.*
538 *Express* **20**(5), 5613 (2012) [doi:10.1364/OE.20.005613].
- 539 4. M. Khaleghi et al., “Digital holographic measurements of shape and 3D sound-induced
540 displacements of Tympanic Membrane.,” *Opt. Eng.* **52**(10), 101916 (2013)
541 [doi:10.1117/1.OE.52.10.101916].
- 542 5. S. Van der Jeught, J. Soons, and J. J. J. Dirckx, “Real-time microscopic phase-shifting
543 profilometry,” *Appl. Opt.* **54**(15), 4953–4959 (2015).
- 544 6. K. Gurusamy, K. Samraj, and B. R. Davidson, “Three dimensional versus two

- 545 dimensional imaging for laparoscopic cholecystectomy,” in Cochrane Database of
546 Systematic Reviews(1) (2008) [doi:10.1002/14651858.CD006882].
- 547 7. R. C. W. Bell and J. G. Price, “Laparoscopic inguinal hernia repair using an anatomically
548 contoured three-dimensional mesh,” *Surg. Endosc. Other Interv. Tech.* **17**(11), 1784–1788
549 (2003) [doi:10.1007/s00464-002-8763-4].
- 550 8. N. J. Durr, G. Gonzalez, and V. Parot, “3D imaging techniques for improved
551 colonoscopy,” *Expert Rev. Med. Devices* **11**(2), 105–107 (2014)
552 [doi:10.1586/17434440.2013.868303].
- 553 9. S. Ieiri et al., “Augmented reality navigation system for laparoscopic splenectomy in
554 children based on preoperative CT image using optical tracking device,” *Pediatr. Surg. Int.*
555 **28**(4), 341–346 (2012) [doi:10.1007/s00383-011-3034-x].
- 556 10. M. E. Hurley et al., “Three-dimensional Volume-rendered Helical CT before
557 Laparoscopic Adrenalectomy,” in *Radiology* **229**(2), pp. 581–586 (2003)
558 [doi:10.1148/radiol.2292021390].
- 559 11. A. Schneider et al., “Augmented reality assisted laparoscopic partial nephrectomy.,” *Med.*
560 *Image Comput. Comput. Assist. Interv.* **17**(Pt 2), 357–364 (2014).
- 561 12. L. M. Su et al., “Augmented Reality During Robot-assisted Laparoscopic Partial
562 Nephrectomy: Toward Real-Time 3D-CT to Stereoscopic Video Registration,” *Urology*
563 **73**(4), 896–900 (2009) [doi:10.1016/j.urology.2008.11.040].
- 564 13. A. F. Durrani and G. M. Preminger, “Three-dimensional video imaging for endoscopic
565 surgery,” *Comput. Biol. Med.* **25**(2), 237–247 (1995) [doi:10.1016/0010-4825(95)00001-
566 K].
- 567 14. A. Tabae et al., “Three-dimensional endoscopic pituitary surgery,” *Neurosurgery*

- 568 **64**(SUPPL. 5) (2009) [doi:10.1227/01.NEU.0000338069.51023.3C].
- 569 15. D. Stoyanov et al., “Real-time stereo reconstruction in robotically assisted minimally
570 invasive surgery,” in Lecture Notes in Computer Science (including subseries Lecture
571 Notes in Artificial Intelligence and Lecture Notes in Bioinformatics) **6361 LNCS**(PART
572 1), pp. 275–282 (2010) [doi:10.1007/978-3-642-15705-9_34].
- 573 16. N. T. Clancy et al., “Spectrally encoded fiber-based structured lighting probe for
574 intraoperative 3D imaging,” *Biomed. Opt. Express* **2**(11), 3119–3128 (2011)
575 [doi:10.1364/BOE.2.003119].
- 576 17. C. Schmalz et al., “An endoscopic 3D scanner based on structured light,” *Med. Image*
577 *Anal.* **16**(5), 1063–1072 (2012) [doi:10.1016/j.media.2012.04.001].
- 578 18. M. Hayashibe, N. Suzuki, and Y. Nakamura, “Laser-scan endoscope system for
579 intraoperative geometry acquisition and surgical robot safety management,” *Med. Image*
580 *Anal.* **10**(4), 509–519 (2006) [doi:10.1016/j.media.2006.03.001].
- 581 19. P. Mountney, D. Stoyanov, and G. Z. Yang, “Three-dimensional tissue deformation
582 recovery and tracking,” in *IEEE Signal Processing Magazine* **27**(4), pp. 14–24 (2010)
583 [doi:10.1109/MSP.2010.936728].
- 584 20. D. J. Mirota, M. Ishii, and G. D. Hager, “Vision-based navigation in image-guided
585 interventions,” *Annu. Rev. Biomed. Eng.* **13**, 297–319 (2011) [doi:10.1146/annurev-
586 bioeng-071910-124757].
- 587 21. N. Bedard et al., “Light field otoscope,” *Imaging Appl. Opt.*, IM3C.6 (2014).
- 588 22. A. J. Das et al., “A compact structured light based otoscope for three dimensional imaging
589 of the tympanic membrane,” in *Proc. SPIE 9303*, p. 93031F (2015)
590 [doi:10.1117/12.2079761].

- 591 23. M. H. McDonald et al., “New insights into mechanism of Eustachian tube ventilation
592 based on cine computed tomography images,” *Eur. Arch. Oto-Rhino-Laryngology* **269**(8),
593 1901–1907 (2012) [doi:10.1007/s00405-011-1829-y].
- 594 24. S. Zhang, “Recent progresses on real-time 3D shape measurement using digital fringe
595 projection techniques,” *Opt. Lasers Eng.* **48**(2), 149–158 (2010)
596 [doi:10.1016/j.optlaseng.2009.03.008].
- 597 25. S. Van der Jeught and J. J. J. Dirckx, “Real-time structured light profilometry: a review,”
598 *Opt. Lasers Eng.*, 1–14, Elsevier (2016) [doi:10.1016/j.optlaseng.2016.01.011].
- 599 26. S. Zhang and S.-T. Yau, “High-speed three-dimensional shape measurement system using
600 a modified two-plus-one phase-shifting algorithm,” in *Optical Engineering* **46**(11), p.
601 113603 (2007) [doi:10.1117/1.2802546].
- 602 27. S. Van der Jeught, J. Sijbers, and J. Dirckx, “Fast Fourier-Based Phase Unwrapping on the
603 Graphics Processing Unit in Real-Time Imaging Applications,” *J. Imaging* **1**(1), 31–44
604 (2015) [doi:10.3390/jimaging1010031].
- 605 28. Y. Xu et al., “Phase error compensation for three-dimensional shape measurement with
606 projector defocusing,” *Appl. Opt.* **50**(17), 2572–2581 (2011)
607 [doi:10.1364/AO.50.002572].
- 608 29. B. T. Phong, “Illumination for computer generated pictures,” *Commun. ACM* **18**(6), 311–
609 317 (1975) [doi:10.1145/360825.360839].
- 610 30. J. J. J. Dirckx and W. F. Decraemer, “Human tympanic membrane deformation under
611 static pressure,” *Hear. Res.* **51**(1), 93–105 (1991) [doi:10.1016/0378-5955(91)90009-X].
- 612 31. W. Alian et al., “The Effect of Increased Stiffness of the Incudostapedial Joint on the
613 Transmission of Air-Conducted Sound by the Human Middle Ear,” *Otol. Neurotol.* **34**(8),

- 614 1503–1509 (2013) [doi:10.1097/MAO.0b013e3182923ed0].
- 615 32. M. Von Unge et al., “Evaluation of a model for studies on sequelae after acute otitis media
616 in the Mongolian gerbil,” *Acta Otolaryngol.* **129**(3), 261–267 (2009)
617 [doi:10.1080/00016480802239091].
- 618 33. J. J. J. Dirckx et al., “Volume displacement of the gerbil eardrum pars flaccida as a
619 function of middle ear pressure,” *Hear. Res.* **118**(1–2), 35–46 (1998) [doi:10.1016/S0378-
620 5955(98)00025-2].
- 621 34. M. Von Unge et al., “Tympanic membrane displacement patterns in experimental
622 cholesteatoma,” *Hear. Res.* **128**(1–2), 1–15 (1999) [doi:10.1016/S0378-5955(98)00183-
623 X].
- 624 35. T. Ockermann et al., “Balloon dilatation Eustachian Tuboplasty: A clinical study,”
625 *Laryngoscope* **120**(7), 1411–1416 (2010) [doi:10.1002/lary.20950].
- 626 36. V. Van Rompaey et al., “Eustachian tube balloon dilation surgery: current state of the art,”
627 *Tijdschr. Geneesk.* **70**(18), 1052–1059 (2014).

628 **Caption List**

629
630 **Fig. 1** Modified otoscopic unit (I) and schematic overview of its optical layout with enlarged
631 detail of otoscope head (II).

632 **Fig. 2** (color online) Real-time three-step 2+1-phase shifting profilometry timeline. Horizontally
633 aligned blocks occur sequentially; vertically aligned blocks occur simultaneously. At all times,
634 fringe pattern acquisition, digital signal processing and on-screen rendering of successive
635 measurements are executed asynchronously. Following the data processing cycle of one 3D-
636 measurement (blue, diagonally hatched), three input fringe patterns are first captured by the
637 high-speed camera and transferred from CPU to GPU memory. Next, the digital signal

638 processing pipeline performs successive wrapped phase extraction (φ_W), phase unwrapping
639 (φ_U), Gaussian filtering (φ_F), phase-to-height conversion and scaling (z_S) and normal
640 calculation (z_N). Finally, the 3D height map is rendered and displayed.

641 **Fig. 3** The surface profile of a flat glass plate was measured at discrete intervals around the
642 central focal plane $Z = 0$ to determine the measurement precision of the proposed otoscopic
643 system. Cross-sections of these depth measurements along the X -axis (I) and the Y -axis (II) are
644 included in the first row, and the corresponding depth measurement errors (dZ) at object depths
645 of $Z = +4$ mm (red), $Z = 0$ mm (black) and $Z = -4$ mm (blue) are included in the second row.
646 Part III plots the two-dimensional root-mean-square values of the difference between the full flat
647 glass plate measurements and their respective best planar fits in function of object depth.

648 **Fig. 4, Vid. 1** Still frame from live measurement video demonstrating the real-time otoscopic
649 profilometry technique (I), including a cross-section of the object's height profile Z along the
650 central pixel line (II) and its measurement error dZ (III).

651 **Fig. 5** Dynamic tympano-topography measurement setup. The otoscopic profilometer head
652 contains a disposable speculum, which is inserted into the ear canal of an airtight sealed temporal
653 bone. The middle ear cavity is pressurized by connecting a small tube through one of the mastoid
654 cells to a pressure generator (not shown here).

655 **Fig. 6** Various steps of the 2+1 phase shifting profilometry pipeline during measurement of
656 tympanic membrane (left ear, medial view) shape deformation. Parts I-III: input intensity
657 images; Part IV: wrapped phase map; Part V: unwrapped phase map; Part VI: height deformation
658 map.

659 **Fig. 7, Vid. 2** Tympanic membrane height deformation response to dynamic middle ear pressure
660 variation. Height deformation profiles and full-field 2D and 3D deformation maps are included

661 in Parts II, III and IV, respectively. The positive z-axis is defined towards the observer and the
662 colorbar legend defined in Part I applies to Parts III and IV, also.

663

664